Investigation of the influence of sampling schemes on quantitative dynamic fluorescence imaging

YUNPENG DAI,[1,6] XUELI CHEN,[1,3,6] JIPENG YIN,[2,6] GUODONG WANG,[2] BO WANG,[1] YONGHUA ZHAN,[1,4] YONGZHAN NIE,[2] KAICHUN WU,[2] AND JIMIN LIANG[1,5]

[1]*Engineering Research Center of Molecular and Neuro Imaging of Ministry of Education & School of Life Science and Technology, Xidian University, Xi'an, Shaanxi 710071, China*
[2]*State Key Laboratory of Cancer Biology and Xijing Hospital of Digestive Diseases, Xijing Hospital, Fourth Military Medical University, Xi'an 710032, China*
[3]*xlchen@xidian.edu.cn*
[4]*yhzhan@xidian.edu.cn*
[5]*jimleung@mail.xidian.edu.cn*
[6]*These authors contributed equally to this work*

Abstract: Dynamic optical data from a series of sampling intervals can be used for quantitative analysis to obtain meaningful kinetic parameters of probe *in vivo*. The sampling schemes may affect the quantification results of dynamic fluorescence imaging. Here, we investigate the influence of different sampling schemes on the quantification of binding potential (*BP*) with theoretically simulated and experimentally measured data. Three groups of sampling schemes are investigated including the sampling starting point, sampling sparsity, and sampling uniformity. In the investigation of the influence of the sampling starting point, we further summarize two cases by considering the missing timing sequence between the probe injection and sampling starting time. Results show that the mean value of *BP* exhibits an obvious growth trend with an increase in the delay of the sampling starting point, and has a strong correlation with the sampling sparsity. The growth trend is much more obvious if throwing the missing timing sequence. The standard deviation of *BP* is inversely related to the sampling sparsity, and independent of the sampling uniformity and the delay of sampling starting time. Moreover, the mean value of *BP* obtained by uniform sampling is significantly higher than that by using the non-uniform sampling. Our results collectively suggest that a suitable sampling scheme can help compartmental modeling of dynamic fluorescence imaging provide more accurate results and simpler operations.

References and links

1. W. Cai and X. Chen, "Multimodality molecular imaging of tumor angiogenesis," J. Nucl. Med. **49**(Suppl 2), 113S–128S (2008).
2. R. Weissleder, "Molecular Imaging in Cancer," Science **312**(5777), 1168–1171 (2006).
3. L. Cunha, K. Szigeti, D. Mathé, and L. F. Metello, "The role of molecular imaging in modern drug development," Drug Discov. Today **19**(7), 936–948 (2014).
4. L. Zhu, N. Guo, Q. Li, Y. Ma, O. Jacboson, S. Lee, H. S. Choi, J. R. Mansfield, G. Niu, and X. Chen, "Dynamic PET and Optical Imaging and Compartment Modeling using a Dual-labeled Cyclic RGD Peptide Probe," Theranostics **2**(8), 746–756 (2012).
5. V. Bérard, J. A. Rousseau, J. Cadorette, L. Hubert, M. Bentourkia, J. E. van Lier, and R. Lecomte, "Dynamic imaging of transient metabolic processes by small-animal PET for the evaluation of photosensitizers in photodynamic therapy of cancer," J. Nucl. Med. **47**(7), 1119–1126 (2006).
6. S. T. Proulx, Q. Ma, D. Andina, J. C. Leroux, and M. Detmar, "Quantitative measurement of lymphatic function in mice by noninvasive near-infrared imaging of a peripheral vein," JCI Insight **2**(1), e90861 (2017).

7. P. Dupont and J. Warwick, "Kinetic modelling in small animal imaging with PET," Methods **48**(2), 98–103 (2009).
8. K. S. Samkoe, K. Sexton, K. M. Tichauer, S. K. Hextrum, O. Pardesi, S. C. Davis, J. A. O'Hara, P. J. Hoopes, T. Hasan, and B. W. Pogue, "High Vascular Delivery of EGF, but Low Receptor Binding Rate Is Observed in AsPC-1 Tumors as Compared to Normal Pancreas," Mol. Imaging Biol. **14**(4), 472–479 (2012).
9. S. C. Kanick, K. M. Tichauer, J. Gunn, K. S. Samkoe, and B. W. Pogue, "Pixel-based absorption correction for dual-tracer fluorescence imaging of receptor binding potential," Biomed. Opt. Express **5**(10), 3280–3291 (2014).
10. M. Choi, K. Choi, S. W. Ryu, J. Lee, and C. Choi, "Dynamic fluorescence imaging for multiparametric measurement of tumor vasculature," J. Biomed. Opt. **16**(4), 046008 (2011).
11. R. W. Holt, J. L. Demers, K. J. Sexton, J. R. Gunn, S. C. Davis, K. S. Samkoe, and B. W. Pogue, "Tomography of epidermal growth factor receptor binding to fluorescent Affibody in vivo studied with magnetic resonance guided fluorescence recovery in varying orthotopic glioma sizes," J. Biomed. Opt. **20**(2), 026001 (2015).
12. Y. Dai, X. Chen, J. Yin, X. Kang, G. Wang, X. Zhang, Y. Nie, K. Wu, and J. Liang, "Investigation of injection dose and camera integration time on quantifying pharmacokinetics of a Cy5.5-GX1 probe with dynamic fluorescence imaging in vivo," J. Biomed. Opt. **21**(8), 086001 (2016).
13. Y. Dai, J. Yin, Y. Huang, X. Chen, G. Wang, Y. Liu, X. Zhang, Y. Nie, K. Wu, and J. Liang, "In vivo quantifying molecular specificity of Cy5.5-labeled cyclic 9-mer peptide probe with dynamic fluorescence imaging," Biomed. Opt. Express **7**(4), 1149–1159 (2016).
14. M. Muzi, F. O'Sullivan, D. A. Mankoff, R. K. Doot, L. A. Pierce, B. F. Kurland, H. M. Linden, and P. E. Kinahan, "Quantitative assessment of dynamic PET imaging data in cancer imaging," Magn. Reson. Imaging **30**(9), 1203–1215 (2012).
15. J. Xin, X. Zhang, J. Liang, L. Xia, J. Yin, Y. Nie, K. Wu, and J. Tian, "In vivo gastric cancer targeting and imaging using novel symmetric cyanine dye-conjugated GX1 peptide probes," Bioconjug. Chem. **24**(7), 1134–1143 (2013).
16. J. Yin, X. Hui, L. Yao, M. Li, H. Hu, J. Zhang, B. Xin, M. He, J. Wang, Y. Nie, and K. Wu, "Evaluation of Tc-99 m labeled dimeric GX1 peptides for imaging of colorectal cancer vasculature," Mol. Imaging Biol. **17**(5), 661–670 (2015).
17. Y. Dai, X. Chen, J. Yin, X. Kang, G. Wang, X. Zhang, Y. Nie, K. Wu, and J. Liang, "Investigation of injection dose and camera integration time on quantifying pharmacokinetics of a Cy5.5-GX1 probe with dynamic fluorescence imaging in vivo," J. Biomed. Opt. **21**(8), 086001 (2016).
18. M. Ichise, J. H. Meyer, and Y. Yonekura, "An introduction to PET and SPECT neuroreceptor quantification models," J. Nucl. Med. **42**(5), 755–763 (2001).
19. J. Logan, J. S. Fowler, N. D. Volkow, G.-J. Wang, Y.-S. Ding, and D. L. Alexoff, "Distribution volume ratios without blood sampling from graphical analysis of PET data," J. Cereb. Blood Flow Metab. **16**(5), 834–840 (1996).
20. R. B. Innis, V. J. Cunningham, J. Delforge, M. Fujita, A. Gjedde, R. N. Gunn, J. Holden, S. Houle, S.-C. Huang, M. Ichise, H. Iida, H. Ito, Y. Kimura, R. A. Koeppe, G. M. Knudsen, J. Knuuti, A. A. Lammertsma, M. Laruelle, J. Logan, R. P. Maguire, M. A. Mintun, E. D. Morris, R. Parsey, J. C. Price, M. Slifstein, V. Sossi, T. Suhara, J. R. Votaw, D. F. Wong, and R. E. Carson, "Consensus nomenclature for in vivo imaging of reversibly binding radioligands," J. Cereb. Blood Flow Metab. **27**(9), 1533–1539 (2007).
21. K. S. Samkoe, K. Sexton, K. M. Tichauer, S. K. Hextrum, O. Pardesi, S. C. Davis, J. A. O'Hara, P. J. Hoopes, T. Hasan, and B. W. Pogue, "High vascular delivery of EGF, but low receptor binding rate is observed in AsPC-1 tumors as compared to normal pancreas," Mol. Imaging Biol. **14**(4), 472–479 (2012).
22. Q. G. de Lussanet, S. Langereis, R. G. Beets-Tan, M. H. van Genderen, A. W. Griffioen, J. M. van Engelshoven, and W. H. Backes, "Dynamic contrast-enhanced MR imaging kinetic parameters and molecular weight of dendritic contrast agents in tumor angiogenesis in mice," Radiology **235**(1), 65–72 (2005).
23. N. Hamzei, K. S. Samkoe, J. T. Elliott, R. W. Holt, J. R. Gunn, T. Hasan, B. W. Pogue, and K. M. Tichauer, "Comparison of kinetic models for dual-tracer receptor concentration imaging in tumors," Austin J. Biomed. Eng. **1**, 1 (2014).
24. K. Chen, L.-P. Yap, R. Park, X. Hui, K. Wu, D. Fan, X. Chen, and P. S. Conti, "A Cy5.5-labeled phage-displayed peptide probe for near-infrared fluorescence imaging of tumor vasculature in living mice," Amino Acids **42**(4), 1329–1337 (2012).
25. L. Zhu, N. Guo, Q. Li, Y. Ma, O. Jacboson, S. Lee, H. S. Choi, J. R. Mansfield, G. Niu, and X. Chen, "Dynamic PET and optical imaging and compartment modeling using a dual-labeled cyclic RGD peptide probe," Theranostics **2**(8), 746–756 (2012).
26. M. Laruelle, M. Slifstein, and Y. Huang, "Positron emission tomography: imaging and quantification of neurotransporter availability," Methods **27**(3), 287–299 (2002).
27. C. A. Salinas, G. E. Searle, and R. N. Gunn, "The simplified reference tissue model: model assumption violations and their impact on binding potential," J. Cereb. Blood Flow Metab. **35**(2), 304–311 (2015).
28. R. V. Parsey, M. Slifstein, D. R. Hwang, A. Abi-Dargham, N. Simpson, O. Mawlawi, N. N. Guo, R. Van Heertum, J. J. Mann, and M. Laruelle, "Validation and Reproducibility of Measurement of 5-HT1A Receptor Parameters with [carbonyl-11C]WAY-100635 in Humans: Comparison of Arterial and Reference Tisssue Input Functions," J. Cereb. Blood Flow Metab. **20**(7), 1111–1133 (2000).
29. J. Logan, J. S. Fowler, N. D. Volkow, Y. S. Ding, G. J. Wang, and D. L. Alexoff, "A strategy for removing the bias in the graphical analysis method," J. Cereb. Blood Flow Metab. **21**(3), 307–320 (2001).

1. Introduction

Fluorescence imaging (FI), as one of important branches of molecular imaging technology, has attracted much more attentions and provided an important tool for early diagnosis and staging of cancer [1–3]. Traditional static FI that acquires fluorescent images at the time point of the probe reaching a state of equilibrium can qualitatively describe the location and distribution of the tumor. Especially, combing with tomographic technique, it can provide accurate quantitative information of tumor, such as the three-dimensional localization and volume size. However, static FI cannot provide the dynamic status of the tumor. Combing with kinetics analysis, dynamic FI can estimate various parameters associated with metabolic rate and receptor density. Further combining with singular value decomposition (SVD) analysis, dynamic FI can separate specific signals from non-specific ones, which further improves the accuracy of quantifying the binding potential of a targeted probe [4].

However, sampling schemes may affect the quantification results of dynamic FI, including the sampling starting point, sampling sparsity, and sampling uniformity. To be exact, the timing of the probe injection should be used as the sampling starting point, which can be accomplished with the help of caudal venous catheterization [5–7]. This would significantly increase the complexity of experimental operation, especially for a larger number of animals used in the longitudinal study. It is necessary to affirm whether the acquisition at the timing of the probe injection is needed. Especially when we are only interested in some robust kinetic parameters, such as the binding potential (BP), a receptor density-related parameters. If we can get relatively robust dynamic parameters in case of missing some time points immediately after the injection of the probe, the experimental operations can be much simpler. In current dynamic FI, the sampling sparsity and sampling uniformity were usually empirically determined [8–13]. Too small a sampling interval results in heavier camera burden and data processing burden, but too large a sampling interval results in an unsatisfactory recovery of the time activity curve (TAC), which may affect the accuracy of the determination of kinetic parameters. Considering the decay of radionuclides, non-uniform sampling was usually employed in dynamic PET imaging to ensure the accuracy of the TAC and the quality of dynamic PET images [14]. In such scheme, intensive sampling points were adopted in the primary stage of probe metabolism, and sparse sampling points were used in the latter stage. However, such characteristic becomes different in dynamic FI, because the decay factor can be neglected due to the stability of fluorescent dye [15]. From this point of view, the uniformity and the scale of the sampling interval are probably worth investigating.

Here, we take the quantification of the BP values as an example to investigate the influence of different sampling schemes on quantification of dynamic FI. Logan graphical analysis with reference tissue model (GARTM) combined with SVD are used to calculate the BP values. Based on three groups of sampling schemes including the sampling starting point, sampling sparsity, and sampling uniformity, we design the corresponding investigation experiments. All of the investigations are conducted with the theoretically simulated and experimentally measured data.

2. Materials and methods

2.1 Materials

Athymic female nude BALB/c mice (4-6 weeks, 18-22 g) were obtained from the Laboratory Animal Center of Fourth Military Medical University (FMMU). Cy5.5-GX1 synthesized by FanBo Co. Ltd. (Beijing, China) and its characterization had been done in our previous work [13].

2.2 Xenografted mouse model

All the animal studies were performed in accordance with the FMMU animal protocol. The tumor was introduced by injecting $2 * 10^6$ BGC-823 gastric cancer cells into the subcutaneous area on the right limb of mice. Then it was allowed to grow for about two weeks before imaging. At that time, the tumor size was about 8-10 mm in diameter [16]. Ten mice were randomly divided into two groups (blocked group and unblocked group) according to whether the free GX1 was pre-injected before the injection of imaging probe (Cy5.5-GX1).

2.3 Dynamic fluorescence images

Dynamic fluorescence images were acquired using the IVIS Kinetic imaging system (PerkinElmer, USA). After collecting five background images, the Cy5.5-GX1 was intravenously injected with a dose of 2 nmol [17]. Then, we collected dynamic fluorescent images for 63 minutes immediately after the injection of the probe. The imaging interval and camera integration time were set to be 18 s and 1 s. During data acquisition process, the mice were anesthetized with isoflurane and a thermostat-controlled thermal heater kept their body temperature. In addition, the fluorescent images of each mice were acquired once again after 24 hours of the probe injection.

2.4 Kinetic models and parameter estimation

A two-tissue (three-compartment) model and a one-tissue (two-compartment) model were used to describe tracer kinetics in the tumor region and reference region, respectively [18]. Detailed description of kinetic models and related parameters can be found in [13]. Here, the GARTM model was applied to calculate the *BP* values, which can be expressed as Eq. (1) [19]:

$$\frac{\int_0^T ROI(t)dt}{ROI(T)} = DVR \frac{\int_0^T ref(t)dt + ref(T)/k_2^{ref}}{ROI(T)} + int' \qquad (t > t^*) \qquad (1)$$

where *ROI(t)* and *ref(t)* represent the fluorescent activity in the tumor and reference regions respectively, k_2^{ref} denotes the washout rate from interstitial space into plasma in the reference region, *DVR* represents volume ratio of distribution and int' is a constant. According to the definition of the GARTM model, the value of $\int_0^T ROI(t)dt / ROI(T)$ as a function of $(\int_0^T ref(t)dt + ref(T)/k_2^{ref})/ROI(T)$ will become linear with a slope given by *DVR* when the tracer is injected for a certain period *(t>t*)*. The *BP* values, as a macro-parameter reflecting the binding affinity and the available receptor density, could be calculated as *BP = DVR-1* [20].

2.5 Simulations

Simulations were performed to simulate the uptake process of Cy5.5-GX1. By assuming that the plasma input function is similar to that of IRDye800CW-EGF, we chose the plasma input function of Cy5.5-GX1 from blood sampling experiments published previously [21]. Considering the molecular weight of Cy5.5-GX1 was about 2k Da [22, 23], the kinetic rates constants K_1 and k_2 were set to be 0.013 min^{-1} and 0.13 min^{-1}. The k_3 and k_4 were simply set to be 0.07 min^{-1}, 0.1 min^{-1} in the unblocked group, and 0.02 min^{-1}, 0.1 min^{-1} in the blocked group. To better simulate the actual experimental data, 3% Gaussian noise was added to the simulated tracer uptake curves. The detailed simulation process can be found in the work of Hamzei *et al* [23]. The number of simulations for each group is 10,000 times. All the

simulated time-activity curves (TACs) of fluorescence tracer were interpolated to 9 s intervals from 0 min to 63 min.

2.6 Sampling schemes

Three categories of sampling schemes were designed according to sampling starting point, sampling uniformity and sampling sparsity. In the scheme of sampling starting point, there are two ways for data acquisition, the deferred data acquisition and the truncated data acquisition. By assuming that the probe injection time was 0 min and the actual data acquisition time was T0 min, the deferred data acquisition ignored the data in the period of 0 min to T0 min and directly used the data in the period of T0 min to (60 + T0) min for quantification. However, the truncated data acquisition used the data in the period of 0 min to 60 min for quantification, and the uncollected data in the period of 0 min to T0 min was recovered using the linear interpolation method. For simplicity, the symbol D represents the deferred data acquisition and T denotes the truncated data acquisition. In this work, we set up six sampling starting points, including 0 s, 36 s, 72 s, 108 s, 144 s, and 180 s. In the scheme of sampling uniformity, there are also two ways for data acquisition, uniform acquisition and non-uniform acquisition. In the way of non-uniform acquisition, the data acquisition process was segmented into three sections. Similarly, the symbol U represents the uniform acquisition and N denotes the non-uniform acquisition. In the scheme of sampling sparsity, we designed four sparsity levels that used different number of sampling points, including 200, 100, 50, and 40. The four sparsity levels were simplified as S1 to S4. The detailed definitions of sampling schemes are summarized in Table 1. For better understanding, we take an example to illustrate the meanings of abbreviations. For example, the sampling scheme of UD-S1 (54 s) refers to the uniform acquisition in informality and the first level in sparsity (Table 1, 18 s* 200), and the deferred data acquisition was adopted with the sampling starting point of 54 s.

Table 1. The definitions of different sampling schemes for sampling uniformity and sparsity.

Uniformity / Sparsity	Uniform acquisition (U)	Non-uniform acquisition (N)
Sparsity 1 (S1)	18 s * 200	9 s * 60, 18 s * 80, 27 s * 60
Sparsity 2 (S2)	36 s * 100	18 s * 30, 36 s * 40, 54 s * 30
Sparsity 3 (S3)	72 s * 50	36 s * 15, 72 s * 20, 108 s * 15
Sparsity 4 (S4)	90 s * 40	54 s * 18, 90 s * 13, 162 s * 9

2.7 Image and data analysis

Identification of the regions of interest (ROIs) with the same surface area in the tumor and muscle region was accomplished with Living Image 4.5 software (PerkinElmer, USA). Dynamic fluorescence data pre-processing and analysis were performed using MATLAB 2015b (The MathWorks, USA). The region of muscle contralateral to the tumor was selected as the reference region because of its negligible specific binding [24]. The mean values of fluorescent signals ($*10^6$ photon/cm^2/s) in each ROI were calculated after the average of five background images was subtracted, which were used to determine the TACs within the tumor and muscle ROIs. The singular value decomposition (SVD) method was used to process the acquired fluorescence data to un-mix the specific signals before applying GARTM [25]. In addition, all curves were interpolated to 9 s temporal resolution in order to match the sampling scheme.

2.8 Statistic

Pharmacokinetic parameters were expressed as their mean values and standard deviation (*means ± SD*, *N* = 5). SPSS software (IBM, USA) was employed to conduct all of the

statistical analyses. Statistical significance was evaluated using one-way ANOVA, LSD, and Student's t-test. P values smaller than 0.05 were considered to be of statistically significant difference.

3. Results

3.1 Dynamic fluorescence images and time–activity curves

Figure 1(A) and 1(B) showed the representative raw fluorescent images of the unblocked and blocked groups at 63 min post-injection of probe, respectively. Under the same dynamic display scale, there are obvious fluorescent signals inside the tumor for the unblocked group, but almost invisible in the blocked group. Figure 1(C) and 1(D) plot the pure TACs in the regions of tumor and muscle recovered by SVD analysis for both groups.
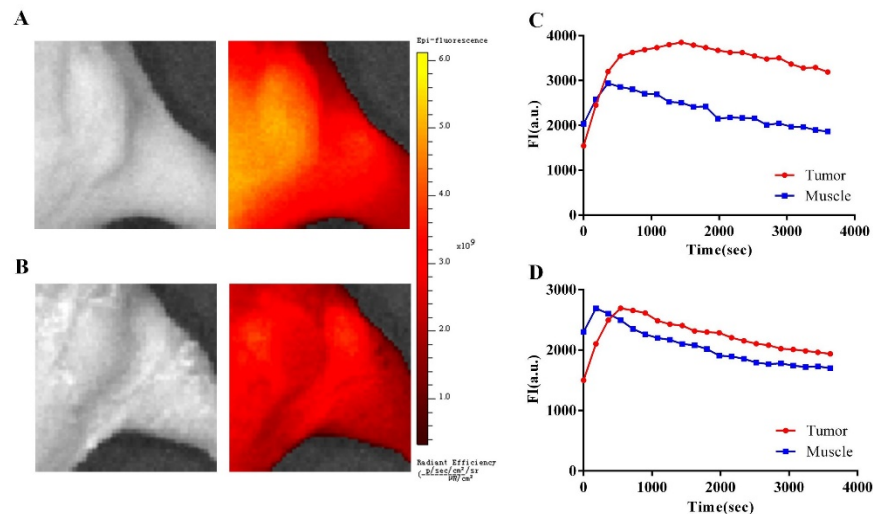

Fig. 1. Dynamic fluorescence images and time–activity curves. Representative raw white light and fluorescent images of unblocked group (A) and blocked group (B) at 63 min post-tracer injection of probe. The corresponding pure TACs of tumor and muscle ROIs obtained by the SVD analysis for the unblocked group (C) and blocked group (D).

3.2 Influence investigation of sampling starting point

We first used simulation data to investigate the influence of sampling starting point on quantification of BP values. Considering the fact that the sampling uniformity and the sampling sparsity would not affect the conclusion, we here only summarized the statistical results of UD-S1 and UT-S1 groups. Figure 2(A) and 2(B) show the estimated BP values for different sampling starting points in the unblocked group and the blocked group respectively. We find that the BP value increased with an increase of T0 for both data acquisition ways. Furthermore, such increasing trend was much faster for the deferred data acquisition than that of the truncated data acquisition. We further statistically analyzed the simulation data, and find that significantly statistical differences can be observed from the second sampling starting point (LSD, $P < 0.05$) in the UD-S1 group. However, such significantly statistical differences were not observed until the third sampling starting point (LSD, $P < 0.05$) in the UT-S1 group. The estimated BP values for different sampling starting points in the real experiment were presented in Fig. 2(C) (unblocked) and 2(D) (blocked). The same conclusion can be addressed as that in the simulation. However, there were no significantly statistical differences among all sets of data in both the unblocked and blocked groups (ANOVA, $P > 0.05$). Moreover, we calculated the parametric maps that displayed the BP values at each point in ROI. Figure 2(E) and 2(F) present such parametric maps in the unblocked (2(E)) and

blocked (2(F)) groups for the sampling scheme of UD-S1. No obvious differences were observed with the change of sampling starting point. To estimate the difference quantitatively, we calculated the image structural similarity index (SSIM) between two parametric maps. There was still no difference and the SSIM was 100%.
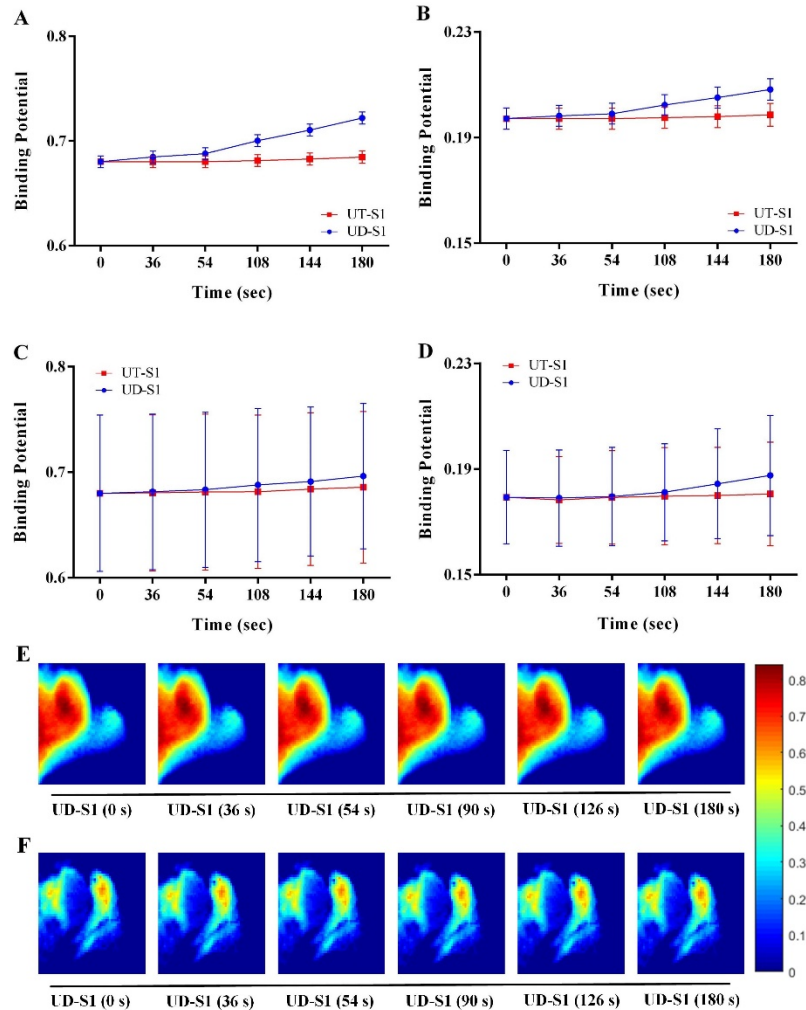

Fig. 2. Influence investigation of different sampling starting points and data acquisition ways on quantification of *BP* values. The *BP* values for different sampling starting points estimated from simulation data in the unblocked group (A) and the blocked group (B). Those estimated from real experiment in the unblocked group (C) and the blocked group (D). The blue curves represent results from the sampling scheme of UD-S1, and the red ones are those of UT-S1. (E) and (F) show the representation parametric maps based on the variation of sampling starting points from the unblocked and blocked groups respectively.

3.3 Influence investigation of sampling uniformity

Similarly, simulations were first conducted to investigate the influence of sampling uniformity on quantification of *BP* values. Figure 3(A) and 3(B) show the estimated *BP* values of different sampling starting points for the sampling schemes of UD-S1 and ND-S1. We find that the *BP* value in the UD-S1 scheme was slightly higher than that in the ND-S1 scheme. However, there was no statistical difference between each pair of data (*t*-test, $P > 0.05$). In other words, at the same conditions of data acquisition way, sampling sparsity, and

sampling starting point, the *BP* value estimated by using the uniform sampling scheme was slightly higher than that obtained by using the non-uniform sampling scheme. Quantification results from the real experiment further confirmed this conclusion. Figure 3(C) and 3(D) show the estimated *BP* values from the real experiment for the unblocked and blocked groups respectively. Almost the same conclusion can be addressed from the real experimental data except that the standard deviations are a little larger. We also calculated the parametric maps for the sampling schemes of UD-S1 (54 s) and ND-S1 (54 s), as shown in Fig. 3(E) (unblocked) and 3(F) (blocked). No obvious differences were observed with the change of sampling uniformity, with the SSIM being of 100%.
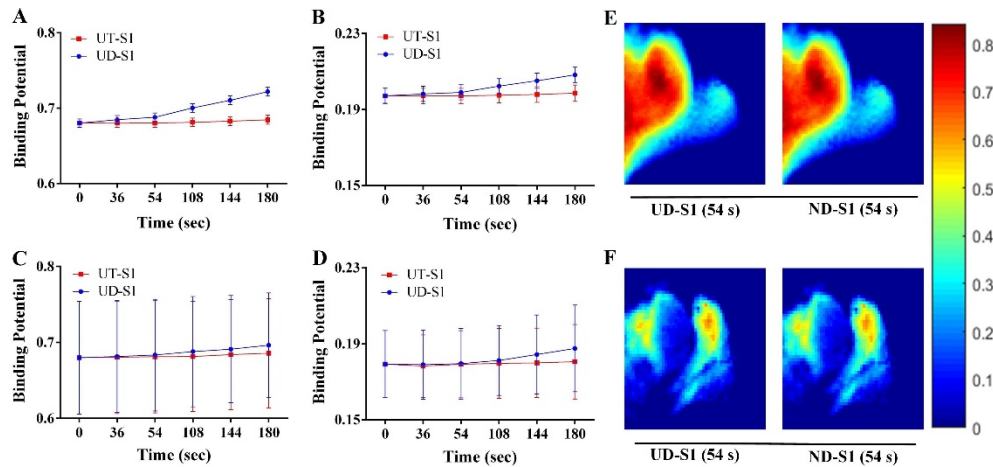

Fig. 3. Influence investigation of sampling uniformity on quantification of *BP* values. The *BP* values for different sampling starting points estimated from simulation data in the unblocked group (A) and the blocked group (B). Those estimated from real experiment in the unblocked group (C) and the blocked group (D). The blue curves represent results from the uniform sampling, and the red ones are those of non-uniform sampling. (E) and (F) show the representation parametric maps at the sampling starting point of 54 s from the unblocked and blocked groups respectively.

3.4 Influence investigation of sampling sparsity

As shown in Fig. 4(A) (unblocked) and 4(B) (blocked), we first used simulation data to investigate the influence of sampling sparsity on quantification of *BP* values. Here, we selected quantification results from the sampling schemes of UD (54 s) and ND (54 s) as examples for results presentation. Two conclusions can be addressed. First, the standard variations of the *BP* values had a tendency to increase with the increase of sampling sparsity in both the unblocked (4(A)) and blocked (4(B)) groups. Second, the mean value of the *BP* values had a tendency to increase with the increase of sampling sparsity in UD (54 s) scheme. However, a trend of rise and fall with the increase of sampling sparsity was observed in ND (54 s) scheme, with the peak point at S3. Further statistical analysis proved that significantly statistical difference can be observed both in the UD (54 s) and ND (54 s) schemes (LSD, $P < 0.05$). Then, real experimental data was further used to verify these conclusions, as shown in Fig. 4(C) (unblocked) and 4(D) (blocked). Statistical analysis results showed that no significantly statistical difference can be observed (ANOVA, $P > 0.05$). Finally, the parametric maps (Fig. 4(E) for the unblocked group, and Fig. 4(F) for the blocked group) showed that no obvious differences were observed with the change of sampling sparsity, with the SSIM being of 100%. It was also obvious that when the other conditions were identical, the *BP* value obtained by the uniform sampling interval was higher than that of the non-uniform sampling interval and the *BP* value obtained by the deferred data acquisition way was higher than that obtained by the truncated data acquisition way.
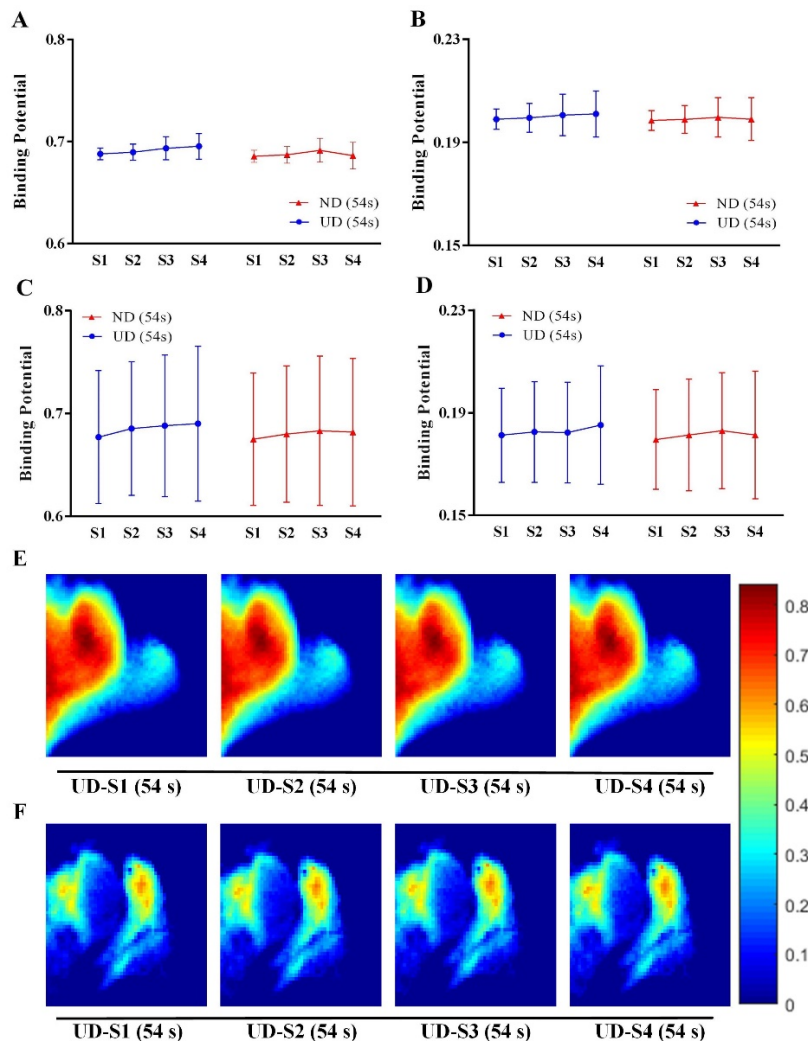
Fig. 4. Influence investigation of sampling sparsity on quantification of *BP* values. The *BP* values for different sampling sparsity level estimated from simulation data in the unblocked group (A) and the blocked group (B). Those estimated from real experiment in the unblocked group (C) and the blocked group (D). The blue curves represent results from the uniform sampling, and the red ones are those of non-uniform sampling. (E) and (F) show the representation parametric maps for different sampling sparsity level at the sampling starting point of 54 s from the unblocked and blocked groups respectively.

To further investigate the trend of quantitative *BP* values with the change of sampling sparsity level, we designed a series of sampling schemes with different number of sampling points. For the sake of simplicity, uniform sampling scheme was used here. This means that the selected sampling points were uniformly distributed on the sampling interval. The quantitated *BP* value as a function of the number of sampling points were shown in Fig. 5, where Fig. 5(A) and 5(B) show the results from the simulation data, and Fig. 5(C) and 5(D) are those from real experiment. We find that the variation of the mean *BP* value became flat when the number of sampling points was greater than 60, which was equivalent to a sampling interval of 1 min. On the other hand, the standard deviation of the *BP* value had a tendency to decrease with the increase of the number of sampling points. Results of the statistical analysis showed that statistical difference can be observed from the simulation data (LSD, all *P* <

0.05) for both the unblocked (Fig. 5(A)) and blocked (Fig. 5(B)) groups, but cannot be found from the real experimental data (ANOVA, all $P > 0.05$).
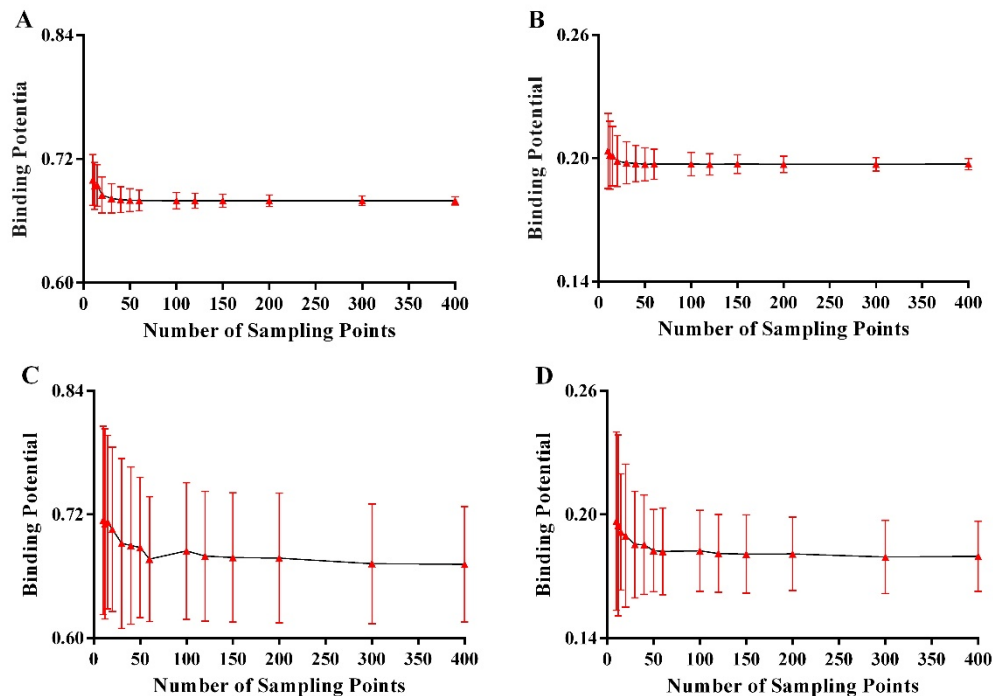

Fig. 5. The estimated *BP* values as a function of the number of sampling points. (A) and (B) are results from the simulation data for the unblocked and blocked groups respectively; (C) and (D) are those from the real experimental data for the unblocked and blocked groups respectively.

4. Discussion

The binding potential (*BP*) of the targeted probe is a very important pharmacokinetics parameter in tumor diagnosis and treatment, because it can reflect the expression level of the available receptors in the tumor [26]. With the ability of analyzing real-time changes of targeted probes *in vivo*, dynamic fluorescent imaging (FI) allows non-invasive quantification of the *BP* values. Incorporating the SVD analysis to un-mix the specific signal component of the tumor from un-specific component, dynamic FI allows *in vivo* quantitative results similar to those of dynamic PET imaging [4]. In this study, based on the GARTM model, we investigated the effects of sampling starting point, sampling uniformity and sampling sparsity on quantification of *BP* values. Currently, there are some limitations in the SVD analysis. Some factors may affect the quantification results, such as the size of ROI, imaging resolution, imaging depth, and signal-to-noise ratio. They are open issues that need to be further studied. Considering the fact that the TACs recovered by the SVD analysis were more consistent with the *in vivo* pharmacokinetics properties of the targeted probe and more similar to the statistical results of the *BP* values of raw data, only the statistical results of the *BP* values obtained by the recovered TACs were displayed.

When investigating two ways of data acquisition, no statistical difference can be observed for the real experimental data. The main reason may be that the variance of the data in the real test is too large. However, the quantitated *BP* values using the truncated data acquisition way is still higher than those using the deferred data acquisition are. This proved that the tail vein catheterization can be avoided to simplify the experimental operations without loss of accuracy of quantitating *BP* values. We only need to record the time of the probe injection

and data acquisition of the first frame. This may lead to another problem. The location of the mice may change slightly before and after the probe injection, which may cause errors in quantification. However, such errors were far less than the signal of the tracer (the difference is multiple magnitude), so that it could be neglected.

When the other conditions were the same, the *BP* values obtained by uniform sampling scheme were higher than those obtained by the non-uniform sampling scheme were. For the GARTM model, the *BP* value is estimated by linear regression of sampling time points discretized in the TACs of the tumor and muscle ROIs. In theory, the greater the difference between the tumor and muscle TACs, the larger the estimated *BP* values. According to the *in vivo* pharmacokinetics properties of the probe, the difference between the tumor and muscle TACs over time will become increasingly large. Thus, compared with the non-uniform sampling scheme, more points were used in the uniform sampling scheme in the late stage when the total sampling points are identical. This is equivalent to further highlighting the proportion of tumor TACs, leading to a higher *BP* value. Currently, there are no gold standard methods for quantifying in vivo receptor concentrations. Each receptor quantitative model has their own advantages and disadvantages. For example, previous studies had found that the *BP* values estimated by the GARTM model was a little small and obtained by the Lammertsma simplified reference tissue model (SRTM) was slightly larger [23, 27–29]. Therefore, when the *BP* value is quantitatively analyzed, it may be possible to improve the accuracy of the *BP* value estimation by choosing a suitable combination of sampling scheme and kinetic quantitative model. Subsequently, the characteristics of several commonly used receptor quantitative model are summarized in Table 2 for reference purposes only [23]. It not only includes the two models abovementioned, but also summarizes the other two models of the reduced full reference tissue model (RFRTM) and the basis function method (BFM).

Table 2. Statistical advantages and disadvantages of the commonly used receptor quantitative model

Model	Advantages	Disadvantages	BP's estimate level
RFRTM	Without assumptions of adiabatic approximation	The slowest fitting speed	Overestimation
SRTM	The most accurate estimates	Specify the proper bounds for the parameters	Slight overestimation
GARTM	The fastest fitting speed	Additional estimate of k2	Underestimation
BFM	More stable in low binding tissues	Pre-specified range for θ3	Underestimation

Similar to the above reasons, the decrease of the number of sampling points makes the *BP* values become larger. The muscle TACs-dominant time quantum is much shorter than that of tumor TACs in the entire 63 minutes of dynamic imaging. The proportional reduction of sampling points is more detrimental to the muscle TACs, leading to the increase of the *BP* values. In the non-uniform sampling scheme, the number of sampling points in the earlier period is more than that used in the uniform sampling scheme. As a result, the growth rate of the *BP* values caused by the proportional reduction of sampling points in the non-uniform sampling scheme is significantly smaller than that in the uniform sampling scheme. When the number of sampling points is the same, the non-uniform sampling scheme in the Sparsity 4 cannot be shrunk with the same proportions as those used in the previous sparsity levels. Thus, we adjusted the segmented nodes of the sampling scheme (equivalent to a lot more in the early stages), which led to the decrease of the *BP* value. This result further proved the above explanation. On the other hand, the standard deviation of the *BP* values became larger as the number of sampling points decreases. This might be caused by the fact that the TACs were more affected by the noise in the integration. As shown in Fig. 5, the variation of the mean *BP* value became very flat when the number of sampling points exceeded 60. This indicated that we should use as many sampling points as possible to improve the estimation accuracy of the *BP* values. From this point of view, this is an advantage of dynamic

fluorescent imaging compared to the current PET dynamic imaging. Higher sampling rate can be used for the dynamic fluorescent imaging to improve the estimation accuracy of the *BP* values while ensuring the quality of dynamic images.

The parametric maps, as shown in Fig. 2-4, were insensitive to the investigated sampling schemes. No obvious differences can be observed with the SSIM being 100%. These results are reasonable, because the influence of the investigated sampling schemes on each pixel of the image is consistent, which will not cause any structural changes. This indicated that we might not consider the investigated sampling schemes if we are only interested in parametric maps. In addition, it was also worth noting that the standard deviation of the *BP* values in the simulation was far less than that in the real experiment. This may be caused by the fact that the individual differences of animals were not considered in the simulations.

In this study, we investigated the influence of different sampling schemes on quantification of *BP* with theoretically simulated and experimentally measured data. The investigated sampling schemes included the sampling starting point, sampling uniformity, and sampling sparsity. Results showed that it is necessary to choose a suitable combination of the kinetic quantitative model and sampling scheme, which may improve the accuracy of the quantitated *BP* values and simplify the experimental operation in dynamic fluorescent imaging. For using the GARTM model to quantify the *BP* values, the preferred sampling schemes are the combination of the truncated data acquisition, uniform sampling, and the sampling sparsity level with the number of sampling points being more than 60. Under such sampling schemes, the procedure of tail vein catheterization can be avoided to simplify the experimental operation in dynamic fluorescent imaging. In summary, our results will provide a valuable reference for the quantification of the *BP* values with the dynamic fluorescence imaging.

Funding

Disclosures

The authors declare that there are no conflicts of interest related to this article.